Pergamon

Available online at www.sciencedirect.com
SCIENCE DIRECT®

Cement and Concrete Research 33 (2003) 1811–1824

CEMENT AND CONCRETE RESEARCH

Investigation of the microstructure of alkali-activated cements by neutron scattering

J.W. Phair[a,*], J.C. Schulz[b,1], W.K. Bertram[c], L.P. Aldridge[c]

[a]Department of Chemical Engineering, University of Melbourne, 3010, Australia
[b]Center for Neutron Research, National Institute of Standards and Technology, Gaithersburg, MD 20899, USA
[c]Australian Nuclear Science and Technology Organization (ANSTO), Menai, NSW, 2334 Australia

Received 22 July 2002; accepted 5 June 2003

Abstract

Significant research has been devoted to understanding and modeling the neutron scattering behavior of Portland cement pastes. The present work examines the potential of neutron scattering to noninvasively evaluate the properties of alternative cementitious materials encountered in the field. To interpret the scattering of both alkali-activated and slag-cement systems, alternative models to those typically adopted for Portland cement pastes were considered. Investigation of alkali-activated and slag-cement coupons were conducted for different sample thickness ($\sim$0.5, 1, 2, 4, 6, 8 and 12 mm) over a wide scattering vector (Q) range ($0.0005 < Q > 0.03$ nm^{-1} and $0.04 < Q > 4$ nm^{-1}) on both ultra (USANS) and conventional small-angle neutron scattering (SANS) spectrometers. This wide Q range allowed determination of the fractal properties of the microstructure as well as the radius of the main scattering particle in the material. An empirical correction for multiple scattering was made based on the Dexter–Beeman equation and demonstrated that for thicker sample widths the theory correlated reasonably well. Alkali-activated fly ash was found to have the largest R value while the OPC and slag mix exhibited the largest Guinier radius. This difference was attributed to variations in the extent of multiple scattering for the samples. Successful application of this model was limited to sample thickness $\geq$1 mm. A combined power law–Sabine expression was also utilized to successfully model the SANS data over a Q range of 0.04–4 nm^{-1}.

Keywords: Microstructure; SANS; Alkali-activated (AA) cement; OPC; XRD

1. Introduction

The purpose of investigating the neutron scattering of cementitious systems is to provide fundamental information that describes the microstructure of cement pastes and to further its application to nondestructive testing of field samples. Techniques such as quasielastic neutron scattering (QENS) and small-angle neutron scattering (SANS) have recently been demonstrated as powerful tools for providing significant new information on the dynamics of the hydration reaction [1–8] and the spatial evolution of the reaction products, respectively [9–11].

Ultimately, it is desirable to correlate these features with material properties and performance on the macroscopic scale as a function of composition, environmental conditions and application. The present work aims to extend neutron scattering analysis to the characterization of alkali-activated cements. To achieve this, reference must firstly be made to the significant work already published utilizing SANS to describe the internal surface and pore structure of Portland cement pastes and ceramic systems [12–14]. This will ensure a more relevant assessment of the scattering properties of alkali-activated cements can be made.

Neutrons are scattered by the force between the atomic nucleus and the neutron, also referred to as the scattering length for a given nucleus [17]. Neutron scattering is therefore strongly dependent upon the phases present in a particular sample, upon the homogeneity of these various phases and the phase contrast between the solid and pores [18]. Scattering in cementitious systems has generally assumed to be dominated by the presence of small particles

* Corresponding author. Present address: Turner-Fairbank Highway Research Center, FHWA, F-211, 6300 Georgetown Pike, McLean, VA 22101, USA.Tel.: +1-202-493-3089; fax: +1-202-493-3086.
E-mail address: john.phair@fhwa.dot.gov (J.W. Phair).
[1] Present address: Bragg Institute, Australian Nuclear Science and Technology Organisation (ANSTO), Menai NSW 2234, Australia.

0008-8846/$ – see front matter © 2003 Elsevier Ltd. All rights reserved.
doi:10.1016/S0008-8846(03)00199-6

or fractal structures as opposed to pores or voids [19]. Since cement is an isotropic system that consists of randomly oriented, independent and nonidentical (polydisperse) scatterers, various methods have been developed to resolve the scattering of these objects.

Considerable work by Allen [9,16,17] and Thomas et al. [2,3,14,15,18] have demonstrated the usefulness of SANS for determining the total surface area of well-defined Portland cement (C_3S or C_2S) paste systems, the water content of the calcium silica hydrate (CSH) phase and for interpreting the microstructure of CSH in terms of a scale-invariant microstructure. In these systems, experimental small angle scattering data of interest has mostly been attributed to the interface between the CSH gel and the cement pore water (under saturated conditions). When admixtures are included within the cement paste such as silica fume, then the interpretation of the SANS spectra must also consider scattering associated with the admixture/matrix interface.

Allen and Livingston [19] have assumed that the scattering associated with particles is negligible with the single most significant scattering feature being the fractal or scale-invariant microstructure structure of the CSH gel. This property may be modeled based on a scattering power law which relates the SANS cross-sectional data to both the distribution of sizes of small spherical globules (between $\sim$0.5 and 100 nm) of CSH, and the fractal agglomerates of the CSH globules. An alternative approach to interpreting small-angle neutron scattering data has been proposed by Sabine et al. [20,21] who suggest that the scattering of hydrated cement pastes is due to the distribution of quasi-spherical objects as opposed to any fractal structure. These objects are of a random size and can be related to the scattering vector by a simple empirical function [21].

Like Portland cement, the main binding constituent in alkali-activated cements is a hydrous gel, albeit, a CSH gel with large quantities of Si substituted for Al [22]. This constituent is very difficult to characterize in situ by conventional experimental techniques. Consequently, SANS provides a potentially new avenue for nondestructively analyzing the dimensions and shape of the binding gel phase within alkali-activated systems.

Clearly, the compositional differences between the hydrous gel of alkali-activated cements and ordinary Portland cements must be considered when interpreting the scattering. Consideration must also extend to properties inherently associated with cement composites and cements containing admixtures, to develop useful mathematical models for interpreting the scattering data. In the present work, the most important factor is the presence of the heterogeneous mineral sources such as fly ash, slag, and kaolin, which extend the particle size distribution of the paste. It is apparent that these admixtures will form numerous new admixture/pore (water) interfaces that will complicate the interpretation of the scattering data.

The increased degree of heterogeneity in these samples is also expected to modify the fractal power laws that have been observed to extend over a wide range of scattering vector (Q) and many decades in intensity in the simpler cement paste system. Nevertheless, in combination with other techniques such as electron microscopy, fractal or scale invariant microstructures can be established to exist in more heterogeneous systems [10,23]. In these instances, fractal properties are still useful since they supply a statistically significant means of characterizing the microstructure of the system even if the individual structures demonstrate fractal or scale invariant behavior over a limited size range [23–26].

The goal, therefore, of the present work is to test and assess the sensitivity of SANS as a meaningful analytical technique for comparing and analyzing the microstructural characteristics of a range of diverse cement pastes. In particular, the SANS spectra of alkali-activated (AA) cements will be compared to a mixture of ordinary Portland cement and ground granulated blast furnace slag (slag). Such a study is novel as neutron scattering investigations of cement to date, have mostly focused on the microstructure of pure Portland cement pastes or phases. No neutron scattering study has yet attempted to investigate the structure of the phases or scattering behavior of alternative cements such as alkali-activated cements.

2. Experimental

Alkali-activated pastes were synthesized from Gladstone Fly ash (QCL) and HR1 kaolin supplied by Commercial Minerals, Sydney, Australia. The chemical oxide composition of these components is presented in Table 1. Particulate properties of the ingredient materials are presented in Table 2. The Brunauer–Emmett–Teller (BET) surface area of the ingredient materials was determined by nitrogen sorption on a Micromeritics ASAP 2000 instrument. Particle size distributions were determined by a Coulter LS130 particle sizer. The cation exchange capacity (CEC) of the ingredient materials was determined following the method of Chapman [27].

Table 1
XRF fusion analysis of the oxide compositions of ingredient materials

Content (%)	Slag	Cement	Fly ash (Gladstone)	Kaolin
Fe_2O_3	0.33	3.41	11.24	1.2
MnO	0.54	0.06	0.17	0.02
TiO_2	0.42	0.22	1.59	2.8
CaO	40.68	63.41	11.24	0.1
K_2O	0.33	0.36	0.5	0.2
SO_3	0.02	0.05	0.46	0
P_2O_5	3.26	2.64	1.02	0.1
SiO_2	33.41	19.92	42.29	52.4
Al_2O_3	14.07	4.51	27.12	28.6
MgO	6.17	1.52	1.41	0.2
Na_2O	0.22	0.45	0.16	0.1

Table 2
Particulate properties of ingredient materials

Property	Fly ash (Gladstone)	Slag	Cement	Kaolin
Surface area (m^2/g)	4.0 ± 0.05	1.6 ± 0.05	8.4 ± 0.05	21.1 ± 0.05
Mean particle size (d_{50}, μm)	14.1 ± 0.03	9.8 ± 0.03	12.6 ± 0.03	0.9 ± 0.03
Density	2.91 ± 0.01	2.33 ± 0.01	2.24 ± 0.01	2.65 ± 0.01
CEC value (meq./100g)	1.3 ± 0.02	9.76 ± 0.03	8.7 ± 0.05	11.6 ± 0.05

Alkali-activated pastes were synthesized as cylinders of height 100 mm and diameter 50 mm. After hand mixing for 5 min, all samples were vibrated for 2 min and set at 45 °C for 24 h before being stored at room temperature for 1 1/2 years at 20 °C. Potassium hydroxide (Orica Aust.) and sodium silicate (PQ Aust.) were used to alkali activate the various pastes. Cementitious pastes based on Portland cement were synthesized from a mixture of slag, Portland cement and water following the same mixing procedure as for alkali-activated pastes. Exact mix compositions of the matrices synthesized are presented in Table 3.

SANS spectra were measured in situ, over various sample thickness for the three pastes on the NG7 30 m SANS [28] and the BT5 Perfect Crystal Diffractometer [29] instruments at the NIST Center for Neutron Research, Gaithersburg, MD. On the NG7 SANS instrument, a neutron wavelength of 0.6 nm was used with spread (fhwm) $\Delta\lambda/\lambda = 0.11$, at two sample to detector distances of 15.3 and 3 m. For experiments on the BT5 ultra small-angle neutron scattering (USANS) instrument, data collection lasted 3 h per sample using a wavelength of 0.24 nm. Sample scattering was corrected for background, empty cell scattering, and individual detector pixel sensitivity. The corrected data sets were circularly averaged and placed on an absolute scale using standard samples and software supplied by NIST [30]. Data reduction for USANS slit-smeared data was performed utilizing additional software provided by NIST [31].

X-ray powder diffractograms (XRD) were obtained using a Phillips PW 1800 diffractometer with CuK_α radiation generated at 20 mA and 40 kV. Specimens were step scanned as random powder mounts from 5–70° 2θ at 0.02° 2θ steps integrated at the rate of 1.2 s per step. Identification of the various crystalline phases in the various alkali-activated and cement composite matrices were achieved through reference to diffraction patterns provided by the Powder Diffraction File of the JCPDS (Joint Committee on Powder Diffraction Standards) data [32].

3. Data analysis

The underlying principle behind the application of SANS is to determine the manner and extent to which a given sample (paste) scatters neutrons relative to the incident neutron beam by virtue of the scattering angle. The scattering is normally represented in terms of the momentum transfer vector, Q:

$$Q = \frac{4\sin(\theta/2)}{\lambda} \quad (1)$$

where λ is the wavelength of the incident neutron beam and θ is the scattering angle. When scattering intensity is represented in terms of the scattering vector it is possible to describe microstructural properties of cementitious pastes. Interpretation of the scattering data of cementitious pastes has relied heavily upon various physical models designed to describe particle size, shape, number and composition present in a two-phase model for the scattering cross section [19].

A number of studies have shown fractal gel microstructures to form in cementitious systems [11,26,33]. However, the definition and terminology used to describe materials exhibiting fractal structures is inconsistent in the literature. The primary source of this discrepancy originates from the various analytical techniques and their subsequent models, used to determine the fractal properties. For SANS fractal analysis, the data is usually modeled in terms of a pair correlation function [10]. Fitting of scattering data for amorphous cementitious systems has been best achieved using a fractal form factor (model) as developed by Sinha et al. [34] or Allen [35]. However, utilizing a highly specific model such as the Allen model for a diverse series of cements is a difficult task since the model was developed to describe Portland cement systems alone. It is therefore necessary to return to the simpler models to allow a more robust fit for heterogeneous and composite cement systems.

When considering small-angle scattering in terms of fractal theory it is important to consider two types of fractal systems in cementitious materials—volume and surface fractals. Volume or mass fractals are a structure (e.g., aggregates of subunits) in which the mass, $M(R)$, within a spherical surface is related by a power dependence to the

Table 3
Mix composition of the alkali-activated and cementitious pastes utilized in the experiments

Ingredient	Proportion (% dry mass)		
Sample	Alkali-activated (AA) fly ash and kaolin	Alkali-activated (AA) fly ash and slag	OPC and slag
Fly ash	59	63	–
H_2O	9.4	10.1	25
KOH	7	–	–
$Na_2O{\cdot}SiO_2$	12.9	13.9	–
Slag	–	12.7	37.5
Cement	–	–	37.5
Kaolin	11.7	–	–
Activator pH	14	12	–

radius, R, of the sphere where r_0 is the size of the primary particle of the fractal structure [36]:

$$M(R) \propto \left(\frac{R}{r_0}\right)^{-D} \tag{2}$$

For the volume fractal structure, denoted using v as subscript for the volume fractal dimension, D_v, it may usually be determined from the gradient of a log–log plot of intensity against Q. This is true whenever $R_c >> Q >> 1/\xi_v$, where, ξ, is the correlation length that describes the size of the structure producing the scattering and R_c, represents the minimum center-to-center distance between fractal structures. A surface fractal, however, represents a region of structure with a mass fractal dimension of 3 that is bounded by a surface, which has a surface fractal dimension (D_s). The surface fractal dimension is normally taken to be equivalent to the gradient of a log–log plot of intensity against Q added to 6, whenever $1/\xi_v >> Q >> 1/\xi_s$ [10,19,36].

In addition to analyzing the data by fractal models, it is useful to interpret any deviations from linear fractal behavior in terms of inherent physical parameters within the systems such as individual growing or shrinking particles that scatter independently. A variety of physical models are available for this purpose including spheres and quasi-spheres [20,21].

Utilization of ultra small-angle neutron scattering (USANS) to supplement conventional SANS allows the measurement of scattering from much larger particles and the modeling of fractal behavior over a much wider Q range. USANS also has the advantage of directly providing the size (R_g) of individual scattering objects through the simple Guinier relationship. Therefore, it is possible to determine the apparent radius of gyration for the gel component of the pastes according to a Guinier fit [37]:

$$I(Q) = I(0)\exp\left(-\frac{R_g^2 Q^2}{3}\right) \tag{3}$$

However, this determination is not without complications as multiple scattering, the inherent experimental phenomenon associated with this technique, reduces the analytical certainty of the measurements. Multiple scattering occurs when the scattered rays from particles in the surface layer act as an incident beam for particles in a subsequent layer, particularly for thick samples. Broadening of the scattering profile and reduction in peak intensity of single scattering events are typical observable consequences of multiple scattering. Consideration must therefore be given to the effects of multiple scattering in order to accurately determine the radius of gyration (or size of any other scattering object) for the scattering phase of alkali-activated and OPC cement coupons.

Considerable work by Barker [38] has generated simple approximation methods to correct data when multiple scattering is prevalent. For systems where refraction effects are unimportant, multiple scattering corrections can be made using power series corrective expressions to characterize the Guinier region of the scattering function. Typically, the scattering function can be fitted to either a Gaussian or spherical model, the Debye–Anderson–Brumberger (DAB) model [39,40], the Sabine model [41] (where the particle shape parameter, p, varies between 2 and 3) or a Lorentzian model given certain fundamental contrast parameters for the sample. From initial observations, it is apparent that the scattering from the present data would most likely be associated with either the spherical or Sabine model. These models could successfully correct for multiple scattering when expressed in a relationship correlating the Guinier radius to the scattering power. However, due to lack of well-defined contrast data for the heterogeneous samples and an inability to completely describe the scattering using the Sabine equation in terms of absolute intensity, alternative approximation methods were investigated.

In the present work, an alternative method of Sabine and Bertram [41] and Aldridge et al. [42] was adopted to correct for multiple scattering allowing more meaningful values for the dimensions of the scattering particle, R, to be determined. Using this method, the scattering particle may be restricted to a specific shape based on describing the SANS intensities by:

$$I(Q) = A\left[1 + \frac{(QR)^2}{3}\right]^{-p} \tag{4}$$

where, Q, is the scattering vector, λ, is the wavelength of the incident neutron beam and θ, is the scattering angle at which the intensity is measured. The particle shape can be defined by the parameter, p, which is 1 for disclike particles or 2 for spherelike particles.

Modeling the effects of multiple scattering can be achieved by following the method of Dexter and Beeman [43] and Schelten and Schmatz [44]. After some algebra and some numerical approximations this yields pinhole SANS intensities,

$$F(Q)^2 = C_t^{-1}\left[\sum_{n=1}^{\infty}\frac{(\sigma t)^n}{n! n^{\alpha}}\left(1 + \frac{R^2Q^2}{3n^{\alpha}}\right)^{-p}\right] \tag{5}$$

whilst for USANS slit geometry

$$F(Q)^2 = C_t^{-1}\left[\sum_{n=1}^{\infty}\frac{(\sigma t)^n}{n! n^{\alpha/2}}\left(1 + \frac{R^2Q^2}{3n^{\alpha}}\right)^{-p-0.5}\right] \tag{6}$$

where, t, is the thickness of the sample, σ, is the cross section per unit volume for coherent elastic scattering and α, is a parameter that depends on the value of p, given by,

$$\alpha = 1.279 + 6.291p^{-5.349} \tag{7}$$

When the normalization constant, C_t, is chosen to make $F(0)^2 = 1$, the intensities from samples of different thickness, t, can be fitted to

$$I_t(Q) = A_t \times F(Q)^2 \tag{8}$$

with,

$$A_t = \frac{1}{2\pi}\left(\frac{2\pi}{\lambda}\right)^2 \frac{2}{3}(p-1)\Phi_0 R C_t e^{-\tau t} \tag{9}$$

where, τ, is the total cross section for removal of neutrons from the incident beam and Φ_0, represents the strength of the incident neutron flux. Subsequently, R, corrected for multiple scattering can then simply be determined by nonlinear least squares fitting of the generalized intensity, $I(Q)$, Eq. (8) above.

4. Results

4.1. X-ray diffraction analysis

Fig. 1 shows the X-ray diffractograms of the three matrices synthesized according to Table 2, with d-spacing values provided for the significant peaks. For both the alkali-activated matrices containing fly ash, a substantial number of peaks could be attributed to the fly ash and its constituent phases. For instance, hematite ($d = 3.42$ Å), quartz ($d = 4.23/5.38$ Å) and mullite ($d = 2.61$ Å) can easily be distinguished as too can amorphous silica, by virtue of a significant hump in the region 15–35° 2θ [45,46]. There was no significant difference between the alkali-activated kaolin and slag mixes except for a few supplementary peaks due to the presence of unreacted kaolin, with a notably stronger peak at a d-spacing of 3.39 Å compared to the slag containing matrix. Both matrices contained peaks at d-spacing values of 3.04 and 2.52 Å which may be assigned to semicrystalline calcium silica hydrate (CSH) and calcium silicate, respectively [47].

In comparison to the paste synthesized solely from ordinary Portland cement and slag, there is a notable absence of peaks associated with quartz ($d = 3.39$ Å) and a variety of other phases associated with fly ash, slag and kaolin starting materials. Significant new peaks may be found with d-spacing values of 2.77, 1.96 and 1.77 Å that can directly be assigned to crystalline phase formation of CSH/calcium silicate, ettringite and calcium silicate, respectively. These products may therefore be directly associated with the presence of Portland cement in the paste. The CSH peak at $d = 3.01$ Å is considerably more intense than the peak observed for the alkali-activated systems. The X-ray diffractograms of the alkali-activated systems both indicate that significant amounts of unreacted starting material within the pastes is present, and this must be accounted for when interpreting SANS data.

4.2. USANS data analysis

USANS slit-smeared data for the matrices prepared according to the proportions in Table 3 are presented in Figs. 2–6 for each sample at varying specimen thickness. Initial examination of the curves demonstrates that they

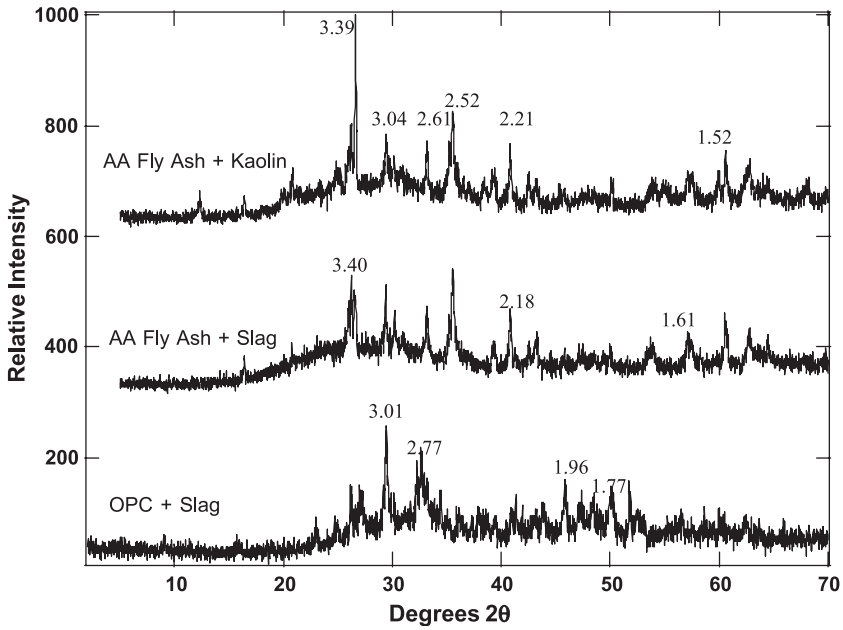

Fig 1. X-ray diffractograms of the three matrices synthesized according to Table 2. d-Spacing values in Å are listed above the significant peaks.

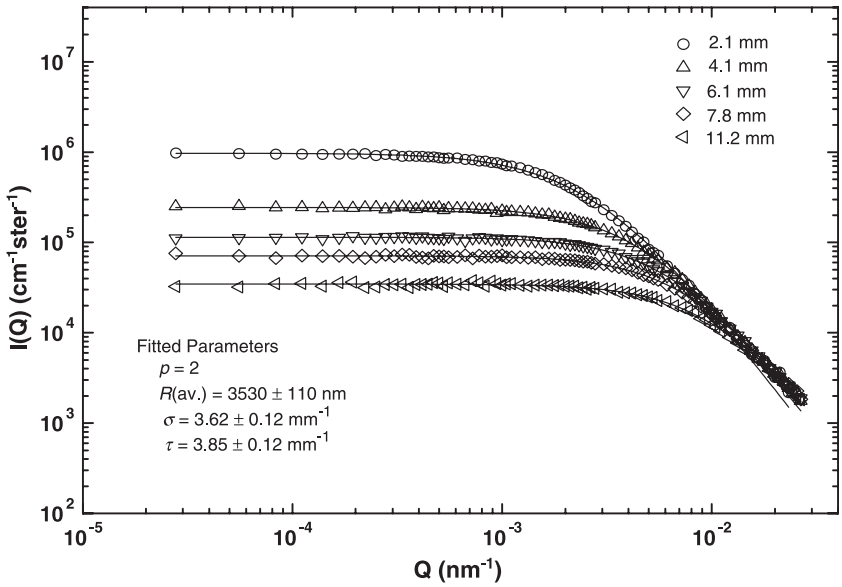

Fig 2. A log–log plot of $I(Q)$ against Q of the USANS slit-smeared data for the thick AA fly ash and kaolin sample as a function of sample thickness. Error bars have been omitted for clarity.

consist mostly of two linear regions with a turn in the curve linking the two regions. The turn occurs at approximately 10^{-2} nm^{-1} for thick samples and approximately 10^{-3} nm^{-1} for the thinner samples. Table 4 lists the average slope of the nonhorizontal linear region for the three different samples, which may be considered in terms of fractal theory through its simplest interpretation as a power law [23,34]. According to Table 4, the slope for the OPC and slag paste (-1.9 ± 0.05) is smaller than they are for the alkali-activated pastes (-2.2 ± 0.05 and -2.9 ± 0.05). The slope may be considered in terms of a volume fractal dimension (D_v) since the scattering here is well within the Porod regime. Accordingly, alkali-activated pastes demonstrate the largest volume fractal dimension with the OPC/slag paste having the smallest volume fractal dimension of 1.9 ± 0.05.

Further analysis of the data may be achieved by quantifying the evolved gel/binding phase within the cement in terms of the size (and shape) of the scattering object. As described earlier, the Guinier radius of individual particles may be determined from the Guinier regime of the scattering data at low angles. Utilization of the BT5 perfect crystal

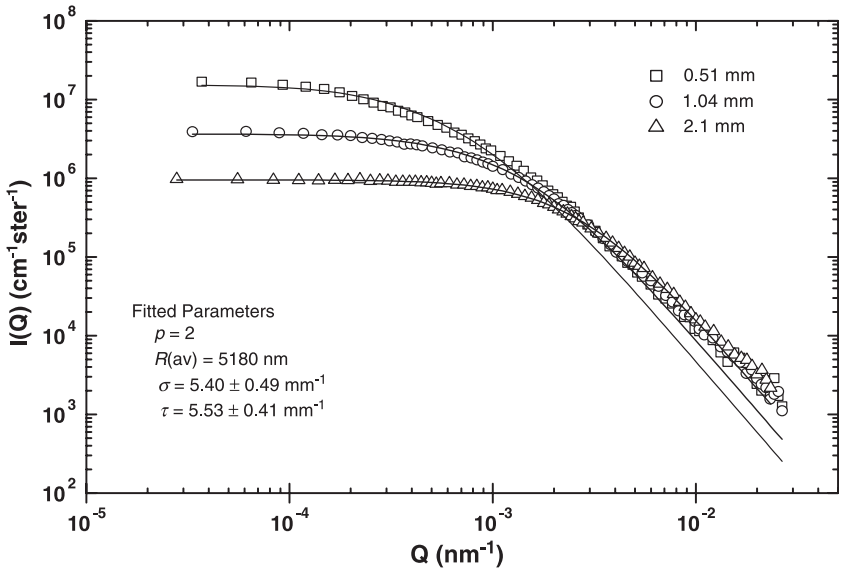

Fig 3. A log–log plot of $I(Q)$ against Q of the USANS slit-smeared data for the thin AA fly ash and kaolin samples as a function of sample thickness. Error bars have been omitted for clarity.

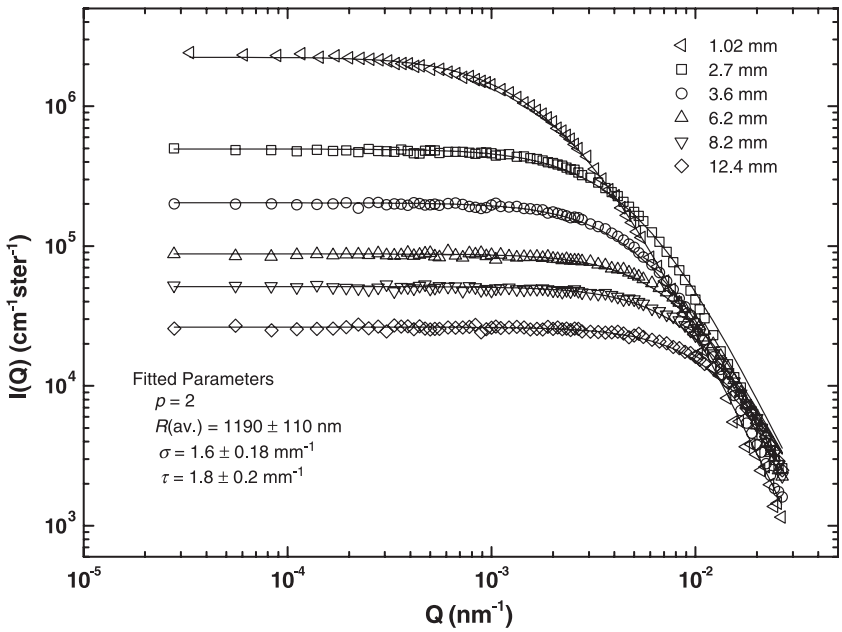

Fig 4. A log–log plot of $I(Q)$ against Q of the USANS slit-smeared data for all AA fly ash and slag samples as a function of sample thickness. Error bars have been omitted for clarity.

diffractometer permits measurement to a much lower Q range than from the conventional SANS making the Guinier region readily observable. The Guinier radius or radius of gyration may be obtained from Eq. (3) as the slope of a $\log[I(Q)]$ vQ^2 plot in the Guinier regime. Fig. 7 presents the apparent Guinier radius for each sample as a function of thickness and clearly demonstrates the effects of multiple scattering through an almost exponential increase in the Guinier radius with decreasing sample thickness on a log $I(Q)$ vs. log Q plot. Furthermore, the OPC/slag sample consistently exhibits the largest Guinier radius followed by alkali-activated fly ash/kaolin, then alkali-activated fly ash/slag as a function of sample thickness.

While the Guinier radius represents the size of a scattering object in terms of a random shape, there exist alternative shapes for interpreting the scattering data that are particu-

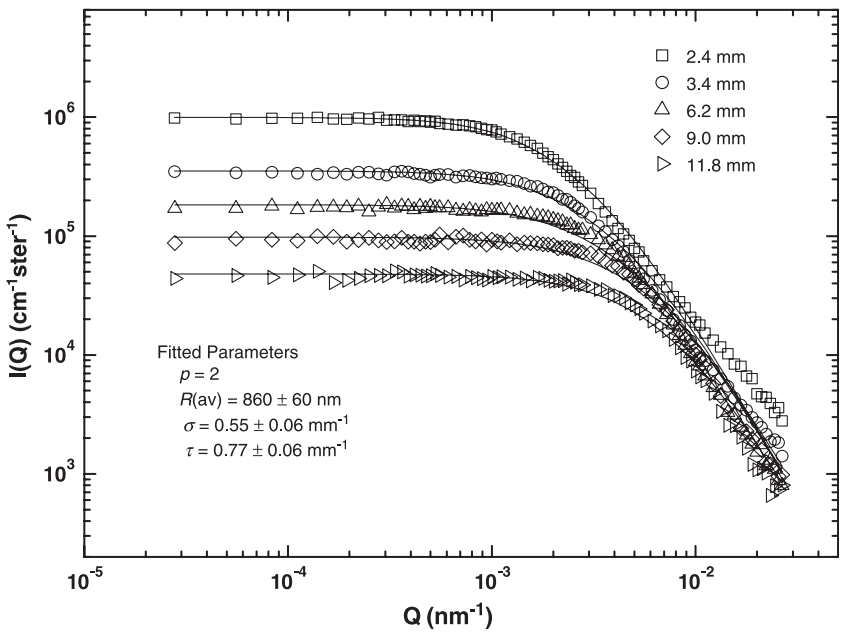

Fig 5. A log–log plot of $I(Q)$ against Q of the USANS slit-smeared data for the thick OPC and slag samples as a function of sample thickness. Error bars have been omitted for clarity.

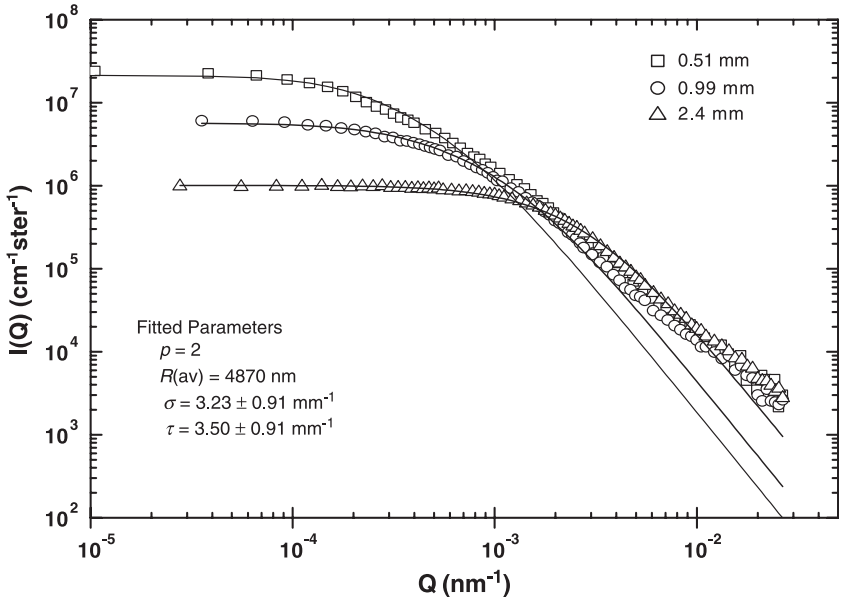

Fig 6. A log–log plot of $I(Q)$ against Q of the USANS slit-smeared data for the thin OPC and slag samples as a function of sample thickness. Error bars have been omitted for clarity.

larly useful for minimizing the negative effects of multiple scattering. Utilization of a sphere for this purpose is an immediate choice given its simplicity and the fact that previous SEM and SANS studies of cementitious systems have shown that the hydration products exhibit spherelike morphology with a diameter around 1 μm [8]. Moreover, previous USANS real-time experiments examining hydrating cement systems have been able to correlate this diameter with the particle size of the hydrating structure surrounding cement particles [41,42]. By asserting that an increase in the spherical scatterer's particle size directly reflects the growth of hydration products, it has subsequently been possible to distinguish between scattering directly attributable to cement particles and new hydration products.

For nonkinetic studies such as the present study, it is not as easy to make such distinctions between the scattering associated with new hydration products and primary structures like undissolved particles. Interpretations may be additionally complicated by the utilization of highly heterogeneous feedstock such as fly ash and slag, which contain particles with diameters of around 1 μm. Therefore, the present work will make the assumption that the measured spherical scattering objects represents the scattering associated with hydration products surrounding reacting particles. Furthermore, XRD data displayed in Fig. 1 indicates that not all of the starting material has completely dissolved so its contribution to the apparent particle size should not be neglected.

Table 4
Average slope of linear region in the log–log plot of intensity vs. Q obtained from the USANS data for each sample presented in Figs. 2–6

Sample	log–log (slope) M ± 0.05	Volume fractal dimension (D_v) ± 0.05
AA fly ash and kaolin	− 2.2	2.2
AA fly ash and slag	− 2.9	2.9
OPC and slag	− 1.9	1.9

4.3. Determination of the radius of the scattering object corrected for multiple scattering

Generally, the presence of multiple scattering in a neutron scattering experiment is to be avoided. However, recent work has suggested that multiple scattering may provide valuable information describing the shape of objects and indicate the absolute value of the contrast between the scattering particles and the matrix [41]. The effects of multiple scattering may be taken into consideration by empirically determining the elastic scattering cross section per unit volume (σ) of the sample as a function of sample thickness (t) where, R, is the spherical particle radius and p, is a factor corresponding to the shape of the particle (see Eq. (6)).

The elastic scattering cross section per unit volume (σ) in the small angle region provides an accurate indication of the amount of material that contributes to the small angle scattering process and can be determined empirically as follows. For each sample, the different thickness specimens can be fitted over a range of σ values. The sum of the square deviation from the mean values of the scattering particle, R, for each of the sample thicknesses can then be plotted as a function of σ, in order to determine the optimum value of σ which occurs where the differences between the fitted radii are least. This provides a value for R that is corrected for

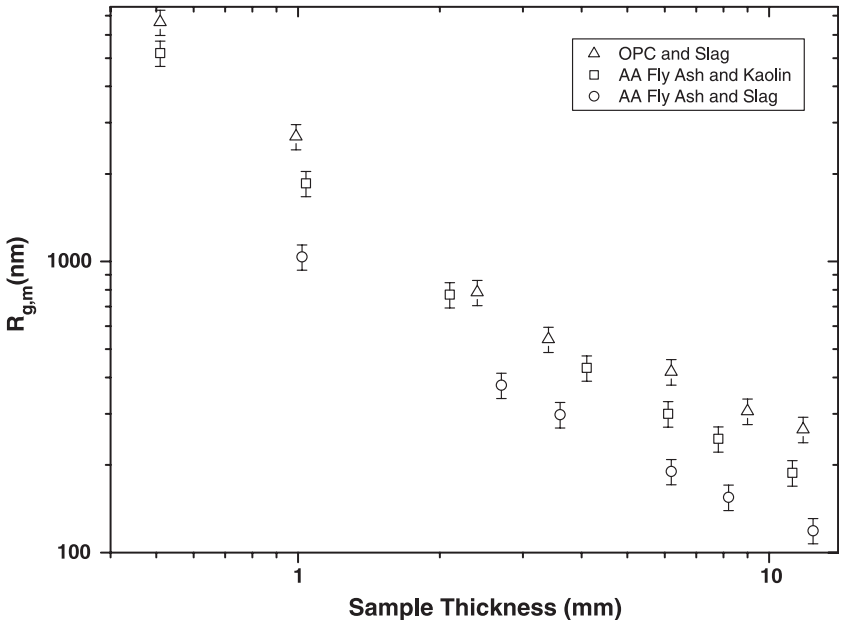

Fig 7. A plot of the apparent Guinier radius (R_g) of the (multiple) scattering particles as a function of sample thickness (mm) for the three samples.

multiple scattering as well as the value for the scattering cross section, τ, and values for A_t. Since both R and σ are now known, it is possible to calculate the normalization constant, C_t. If the theory is to agree with the experimental data, a plot of $\log[A_t/(RC_t)]$ against t should be linear with the resultant slope providing the total cross section, τ.

Figs. 2–6 display the data fits with each curve being fitted to the optimized values of σ, τ and R, for each sample. In most instances, it was necessary to distinguish between values of R determined using all the sample thicknesses, and values of R determined using all the samples except the two thinnest widths of $\sim$0.5 and 1.0 mm. This was necessary for all samples but the alkali-activated fly ash and slag, since no data were collected for it at a thickness of 0.5 mm. The reason why such a distinction is necessary is largely due to the reduced accuracy of the data fits for the very thin samples. Figs. 2, 4 and 5 clearly display accurate data fits for samples thicker than 1 mm. Data fits for the thin samples presented in Figs. 3 and 6, on the other hand, are less satisfactory.

Values for R, corrected for multiple scattering as a function of specimen thickness, are presented for all three samples in Tables 5–7 with and without the thin samples in the analysis. In addition, Table 8 provides the parameters that were used to fit the USANS data presented in Figs. 2–6. By referring to Table 8, it appears that by including the thinner samples in the average corrected values for the radius $R_{av.}$ of the spherical scattering object, its magnitude and error increased significantly. Removing the thin samples from the analysis to consider only those samples to which the theory fits well, produces an $R_{av.}$ value that is substantially lower than both that of the apparent Guinier radius (Fig. 7) and the $R_{av.}$ value determined using all the sample thicknesses. However, the error for $R_{av.}$ for the analysis without the thinner samples is considerably smaller than is observed for the analysis that includes the thinner samples. Meaningful trends amongst the various samples $R_{av.}$ is not

Table 5
Radii of the spherical scattering object, R, corrected for multiple scattering for the alkali-activated fly ash and kaolin matrix, as a function of sample thickness

Thickness (mm) ± 0.05 mm	R value (nm) ± 5 nm	R* value (nm) ± 5 nm
0.51	6119	4820
1.04	5289	3687
2.1	4950	3411
4.1	4856	3411
6.1	4937	3490
7.8	4995	3541
11.2	5142	3655

In analysis of R* values, 0.51 mm thick coupon was not used. R* value for 0.51 mm was obtained using $\sigma = 3.62\ \text{mm}^{-1}$.

Table 6
Radii of the spherical scattering object, R, corrected for multiple scattering for the alkali-activated fly ash and slag matrix, as a function of sample thickness

Thickness (mm) ± 0.05 mm	R value (nm) ± 5 nm
1.02	1285
2.7	1009
3.6	1082
6.2	1173
8.2	1126
12.4	1335

Table 7
Radii of the spherical scattering object, R, corrected for multiple scattering for ordinary Portland cement with slag, as a function of sample thickness

Thickness (mm) ± 0.05 mm	R value (nm) ± 5 nm	R^* value (nm) ± 5 nm
0.51	6948	4953
0.99	4961	2457
2.4	3593	946
3.4	3542	765
6.2	4747	845
9.0	4943	837
11.8	5334	891

In analysis of R^* values, 0.51 and 0.99 mm thick coupons were not used. R^* values for 0.51 and 0.99 mm coupons were obtained using $\sigma = 0.55\ \text{mm}^{-1}$.

straightforward given that they do not include the same sample thicknesses.

Nonetheless, it is still possible to compare the relative magnitude of R determined at a prescribed thickness for the various samples according to Tables 5–7. Generally, the alkali-activated fly ash and kaolin matrix have the largest values followed by the OPC and slag combination and then the alkali-activated fly ash and slag matrix. The exact extent to which the primary structure (refer to XRD Fig. 1 and Table 2) contribute to the corrected particle size requires further investigation.

While there seems to be a significant difference between the sizes of the scattering particles of alkali-activated pastes and ordinary Portland cement pastes, at this stage, there appears to be no major difference in the shape of the scattering particles as a function of sample composition. In theory, it is possible to fit these data to optimize for p but in practice, the errors in the data make it difficult to obtain reliable estimates by normal fitting methods. Thus, the fitting was restricted to using a value of $p = 2$ (spherelike) for the fits. If it were possible to optimize the fitting of p, then it could be used to estimate the fractal D_v.

From the data shown in Table 8 it also appears that the values of the scattering contrast (σ) are considerably different for the three different matrices. There seems to be a strong correlation between the size of the contrast (σ) and the $R_{\text{av.}}$ value with AA fly ash and kaolin being the largest, followed by OPC and slag, then AA fly ash and slag. There was not observed, however, any statistically significant difference in the chemical composition (μ) of the samples.

While Fig. 7 clearly shows how the OPC and slag paste has the largest apparent Guinier radius followed by alkali-activated kaolin and then alkali-activated slag, the relative magnitudes of the scattering objects are altered significantly after correcting for multiple scattering. Tables 5–7 evidently reveal that after correcting for multiple scattering, alkali-activated kaolin now has the largest radius followed by OPC and slag, then alkali-activated slag. This change in relative magnitudes may be explained by the fact that more multiple scattering occurs in the OPC and slag sample relative to the others. In addition, the observed spherical scattering objects in Table 8 are consistently smaller than the apparent Guinier radii in Fig. 5. This demonstrates not only the influence of the shape of the scattering object (random vs. sphere) on the interpretation of the scattering data, but also how the relative differences in multiple scattering greatly affect the apparent size of the particle.

Finally, mention must also be made of the major limitations to the method of Sabine and Bertram [41] for determining the values of τ and R as a function of the sample thickness. The major problem with the application of this model is that strongly multiply scattering data will not converge to a particular particle size. Therefore, all particle sizes larger than the largest particle size obtained by directly fitting the thinnest sample data without multiple scattering can fit the data equally well. Previously, it has been possible to fit scattering data obtained by Hardman-Rhyne and Berk [48] for alumina powder with particle sizes varying over two orders of magnitude (0.3 to 30 μm) to a consistent level of accuracy [38]. However, this was only possible since the contrast, volume fractions and scattering function were known beforehand, providing a parameter to define the scattering power with respect to the particle size.

In the present work, none of the necessary values were available beforehand for such an analysis so the method of Sabine and Bertram was relied upon [41]. Under these circumstances, it is important to have data collected from weakly multiple scattering samples (i.e., thinner samples) to constrain the particle size adequately. Based on USANS transmission measurements, no direct beam component could be observed in the data indicating that an estimated σt value>3 for the thinnest samples (0.5 mm) samples is reasonable. Only when the thin samples were included in the analysis of R could similar values for σt be obtained. While not explicitly detailed here, the samples were also placed in 30/70 mixtures of D_2O/H_2O to reduce the scat-

Table 8
Calculated fitting parameters for the Sabine and Bertram interpretation of the USANS data (±1 S.D.) presented in Figs. 2–6

	AA fly ash and slag	AA fly ash and kaolin		OPC and slag	
		with 0.51 mm	w/o	with 0.51, 0.99 mm	w/o
σ (mm^{-1})	1.6 ± 0.18	5.40 ± 0.49	3.62 ± 0.12	3.23 ± 0.91	0.55 ± 0.06
τ (mm^{-1})	1.8 ± 0.2	5.53 ± 0.41	3.85 ± 0.12	3.50 ± 0.91	0.77 ± 0.06
μ (mm^{-1})	0.20	0.13	0.23	0.27	0.22
$R_{\text{av.}}$ (nm)	1190 ± 110	5180 ± 400	3530 ± 110	4870 ± 1070	860 ± 60

tering by an order of magnitude. Nonetheless, the samples still exhibited significant multiple scattering which would indicate that the value of σt for the thinnest samples may in fact be appreciably larger i.e., $\sigma t > 50$. As a consequence, the actual particle size may indeed be larger than that reported here.

4.4. SANS data fitting

Examination of the coupons was initially conducted on a standard 30m SANS instrument. Before conducting any extensive data fitting, a preliminary data survey was conducted. Fig. 8 presents data for the three pastes defined in Table 3, after conducting a Porod fit to subtract the backgrounds. The thicknesses of the various samples, including the parameters that were used to subtract the background in the Porod fit, are presented in Table 9. Of considerable note, was the magnitude of the Porod constant for the OPC and slag mix compared to that for the alkali-activated systems. This would tend to suggest that the OPC/slag mix has a significantly larger surface area and therefore more convoluted hydration products than either of the alkali-activated samples.

Owing to the highly heterogeneous nature of the samples it was difficult to obtain consistent values for the scattering length density of both the hydrous gel phase and unreacted components for each sample. More rigorous data analysis techniques were therefore unavailable for the present batch of samples. What can be deduced from Fig. 8, however, is that there is a substantial difference between the scattering associated with alkali-activated cements and cements containing slag compared to simpler ordinary Portland cement samples observed here and reported in the literature [14,19]. According to Fig. 8, the log $I(Q)$ vs. log Q plots are essentially linear indicating the systems are largely fractal in nature. Slight deviations from linearity, however, were observed for the alkali-activated samples compared to the OPC/slag mix. To analyze the data a variety of physical models were tried including quasispheres with two different radii, a distribution of spheres with radii following a log-normal distribution, quasispheres plus disk, as well as the fractal parameter following Allen's formula and a Sabine expression combined with a fractal power law.

The method found to interpret all of the data with one equation, follows the novel approach adopted previously by Aldridge et al. [20]. This approach involves fitting the data to the Sabine equation combined with a power law expression to characterize and compare the series of cementitious

Table 9
Experimental parameters (±1 S.D.) obtained for the Porod fit of SANS data displayed in Fig. 6

Sample	Thickness (mm)	Q range ($Å^{-1}$)	BGD ($cm^{-1} st^{-1}$)	Porod constant (10^{36} m^{-5})
AA fly ash and kaolin	0.94	0.15–0.35	0.1605 ± 0.0006	44.5 ± 0.9
AA fly ash and slag	1.02	0.15–0.35	0.0452 ± 0.0005	21.7 ± 0.7
OPC and slag	0.99	0.20–0.36	0.4053 ± 0.0011	129.4 ± 3.7

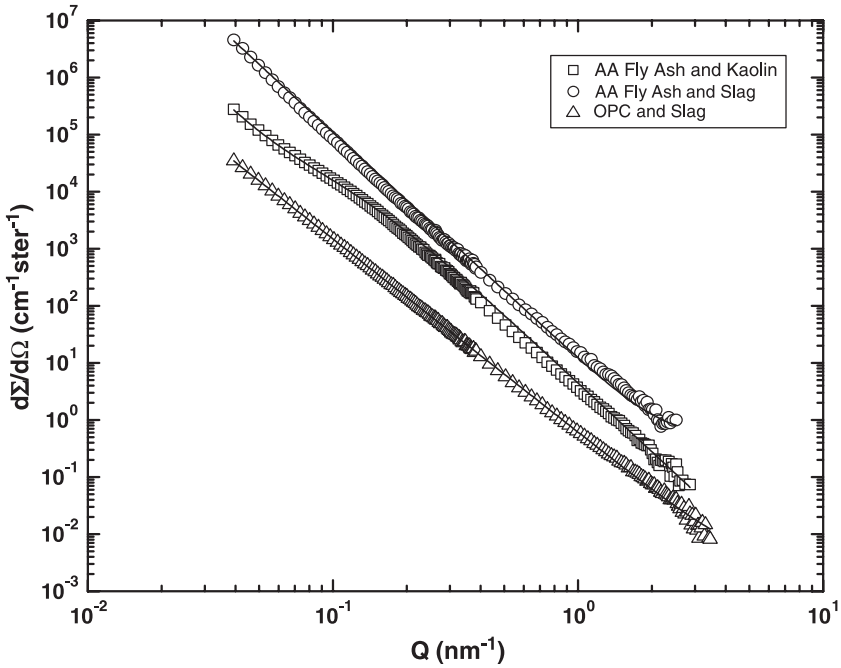

Fig 8. SANS scattering curves of three different matrices defined in Table 2. Curves were fitted with a combined power law and Sabine expression. Error bars have been omitted for clarity.

compounds of various compositions. The combined Sabine–power law expression is given as:

$$I(Q) = \frac{A}{\left(1 + \frac{(QZ)^2}{3}\right)^2} + BQ^{-S} + C \quad (10)$$

where, A and B, are constants, C, is the background count, Z, is the radius of the quasispherical particle and, S, the power law exponential (N.B. For calculation of the surface fractal dimension, $S = 6 - D_s$; while for the volume fractal dimension, $S = D_v$).

As shown by the curves in Fig. 8, this model provides a good fit for a range of pastes of variable compositions. In Table 10, the fit parameters that were used to fit the data in Fig. 8 are provided. The fit parameters demonstrate that the radius of the quasisphere was too large to be accurately determined for the ordinary Portland cement and alkali-activated slag pastes. The alkali-activated fly ash and kaolin mix produced a value for the particle size that corresponds to the slight turn in the curve at approximately $Q = 0.1$ nm^{-1}. It is possible that this particle may be associated with new hydration products or the primary structure. This does not discount, however, the possibility of the hydrated phase consisting of larger particle sizes.

The gradients of the log–log plots displayed in Fig. 8 are substantially different to the gradients of the log–log plots displayed in Figs. 2–6, listed in Table 4. This indicates that the regime revealed by the SANS measurements ($0.04 < Q > 4$ nm^{-1}), is more indicative of the surface fractal dimension as opposed to the volume fractal dimension as revealed by USANS measurements. When one now considers the surface fractal dimensions in Table 10, it appears that the magnitude increases in relative terms that are directly opposite to that which was observed for the volume fractal dimensions (Table 4). Now, it is the ordinary Portland cement and slag mix that exhibits the largest surface fractal dimension while the alkali-activated slag and kaolin pastes have smaller values.

A surface fractal has been defined as an interface that has an area proportional to a power of the size of the device used to measure the area [36]. A smooth surface, therefore, has a surface fractal dimension of 2 while a rough or convoluted surface that fills spaces has a fractal dimension of 3. According to the arguments of Winslow [33], the ordinary Portland cement and slag paste can be considered to exhibit a slightly rougher fractal surface than could be observed for the alkali-activated systems. It is difficult to attribute this roughness to any of the primary structural characteristics (see Table 2), so it is therefore assumed that the observed increase in roughness is related to the formation of more convoluted hydration products.

Table 10
Significant fit parameters used to fit the SANS data displayed in Fig. 6 using the combined Sabine–power law expression

Fit parameter	AA fly ash and kaolin	AA fly ash and slag	OPC and slag
S	−3.6 ± 0.1	−4.0 ± 0.1	−3.4 ± 0.1
D_s	2.4 ± 0.1	2.0 ± 0.1	2.6 ± 0.1
Z	12 ± 1	>1000	>1000

The determination of the main scattering particle size to be beyond the accessible range of conventional SANS measurements suggests that the fractal structure is the most valuable information to be extracted from the experimental data. This restricts fractal models to be the most useful interpretative method for the present data despite that Allen's fractal model could not be applied. It was difficult to correlate the values for D_s and the Porod constant with R values obtained from USANS data. An explanation for this is that in hydrating cement systems, the Porod surface area is typically dominated by the surface area of the hydration (e.g., CSH) gel [10]. This therefore suggests that the R values obtained from USANS are more likely associated with the primary structure of the matrix than with the hydration products/gel features.

At this stage, it remains difficult to physically define the scattering particle observed in the USANS data. The effects of multiple scattering are so substantial that the contributions of the average particle size of the primary structure as well as the newly formed hydration products, are difficult to completely resolve.

5. Conclusion

The results confirm the usefulness of investigating the properties of cementitious matrices based on their neutron scattering and multiple-scattering properties. It establishes the potential for nondestructive field-testing of a wide variety of field samples, by utilizing an empirical interpretative method to analyze the USANS data collected for samples of varying thickness.

Interpreting the USANS data with the method of Sabine and Bertram [41] produces fits that agree with the experimental data for sample thicknesses >1 mm. The theory was less conclusive for thinner samples and produced an average value for the scattering particle size lower than expected unless the thinner samples were included. Notwithstanding, this value for the scattering particle size after correcting for multiple scattering was smaller in magnitude than that of the apparent Guinier radius. According to the corrected R values obtained from the USANS data, alkali-activated kaolin/fly ash had the largest scattering particles while alkali-activated fly ash/slag had the smallest. From USANS, it was also observed that alkali-activated kaolin/fly ash had the largest volume fractal dimension, which correlated well with the observation by conventional SANS, that it had the smaller surface fractal dimension. SANS also established that the OPC/slag hydration gel had the largest surface area and surface fractal dimension, which complemented its smallest volume fractal dimension as determined by USANS.

Analysis of the experimental SANS results highlighted the dominant fractal properties of the cementitious materials in the Q range of 0.04 to 4 nm^{-1}. The SANS spectra of alkali-activated kaolin/fly ash revealed an additional peak whose respective particle size could be quantified by the Sabine–power expression. This expression could fit equally well the linear relationship observed for the OPC/slag paste. It remains an ongoing objective to examine the exact physical significance of the constants used in the Sabine–power expression.

Acknowledgements

The authors wish to recognize the financial support of Australian Nuclear Science and Technology Organization (ANSTO), the Access to Major Facilities Program and the commercial encouragement and support from J.S.J. Van Deventer. Contributions by Dr. J. G. Barker and Dr. A. Allen for data interpretation are greatly appreciated. J.W.P acknowledges the financial support of The University of Melbourne Scholarships Fund and an Australian Institute of Nuclear Science and Engineering (AINSE) postgraduate award. J.C.S. acknowledges support from the National Science Foundation under Agreement No. DMR-9986442.

References

[1] S.A. FitzGerald, J.J. Thomas, D.A. Neumann, R.A. Livingston, A neutron scattering study of the role of diffusion in the hydration of tricalcium silicate, Cem. Conc. Res. 32 (2002) 409–413.
[2] J.J. Thomas, S.A. FitzGerald, D.A. Neumann, R.A. Livingston, State of water in hydrating tricalcium silicate and Portland cement pastes as a measured by quasi-elastic neutron scattering, J. Am. Ceram. Soc. 84 (2001) 1811–1816.
[3] J.J. Thomas, H.M. Jennings, Effects of D_2O and mixing on the early hydration kinetics of tricalcium silicate, Chem. Mater. 11 (1999) 1907–1914.
[4] S.A. Fitzgerald, D.A. Neumann, J.J. Rush, D.P. Bentz, R.A. Livingston, In situ quasi-elastic neutron scattering study of the hydration of tricalcium silicate, Chem. Mater. 10 (1998) 397–402.
[5] S.A. Fitzgerald, D.A. Neumann, J.J. Rush, R.J. Kirkpatrick, X. Cong, R.A. Livingston, Inelastic neutron scattering study of the hydration of tricalcium silicate, J. Mater. Res. 14 (1999) 1160–1165.
[6] R. Berliner, M. Popovici, K. Herwig, H.M. Jennings, J. Thomas, Neutron scattering studies of hydrating cement pastes, Physica, B (Amsterdam) 241–243 (1998) 1237–1239.
[7] F. Haussler, M. Hempel, H. Baumbach, Long-time monitoring of the microstructural change in hardening cement paste by SANS, Adv. Cem. Res. 9 (1997) 139–147.
[8] F. Haussler, F. Eichhorn, S. Roehling, H. Baumbach, Monitoring of the hydration process of hardening cement pastes by small-angle neutron scattering, Cem. Concr. Res. 20 (1990) 644–654.
[9] A.J. Allen, D. Pearson, Porosity and gel structure of cement, Microstruct. Charact. Mater. Non-Microsc. Tech., Proc., Risoe Int. Symp. Metall. Mater. Sci. 5 (1984) 175–180.
[10] R.A. Livingston, Fractal nucleation and growth model for the hydration of tricalcium silicate, Cem. Conc. Res. 30 (2000) 1853–1860.
[11] A. Heinemann, H. Hermann, F. Haussler, SANS analysis of fractal microstructures in hydrating cement paste, Physica, B (Amsterdam) 276–278 (2000) 892–893.
[12] R. Berliner, M. Popovici, K. Herwig, H.M. Jennings, J. Thomas, Neutron scattering studies of hydrating cement pastes, Physica, B 241 (1997) 1237–1239.
[13] R. Berliner, M. Popovici, K.W. Herwig, M. Berliner, H.M. Jennings, J.J. Thomas, Quasielastic neutron scattering study of the effect of water-to-cement ratio on the hydration kinetics of tricalcium silicate, Cem. Conc. Res. 28 (1998) 231–243.
[14] J.J. Thomas, H.M. Jennings, A.J. Allen, The surface area of cement paste as measured by neutron scattering: Evidence for the two C–S–H morphologies, Cem. Concr. Res. 28 (1998) 897–905.
[15] J.J. Thomas, H.M. Jennings, A.J. Allen, The surface area of hardened cement paste as measured by various techniques, Concr. Sci. Eng. 1 (1999) 45–64.
[16] A.J. Allen, S. Krueger, G. Skandan, G.G. Long, H. Hahn, H.M. Kerch, J.C. Parker, M.N. Ali, Microstructural evolution during the sintering of nanostructured ceramic oxides, J. Am. Ceram. Soc. 79 (1996) 1202–1212.
[17] R. Berliner, Neutron diffraction and neutron scattering studies of cement, in: S. Mindess, J. Skalny (Eds.), Materials Science of Concrete, American Ceramic Society, Westerville, OH, 2001, pp. 49–99.
[18] J.J. Thomas, H.M. Jennings, A.J. Allen, Determination of the neutron scattering contrast of hydrated Portland cement paste using H_2O/D_2O exchange, Adv. Cem. Based Mater. 7 (1998) 119–122.
[19] A.J. Allen, R.A. Livingston, Relationship between differences in silica fume additives and fine-scale microstructural evolution in cement based materials, Adv. Cem. Based Mat. 8 (1998) 118–131.
[20] L.P. Aldridge, W.K. Bertram, T.M. Sabine, J. Bukowski, J.F. Young, R.K. Heenan, Small-angle neutron scattering from hydrated cement pastes, Mater. Res. Soc. Symp. Proc. 376 (1995) 471–479.
[21] T.M. Sabine, W.K. Bertram, L.P. Aldridge, A method for interpreting small angle neutron scattering data from quasi-spherical objects, Mater. Res. Soc. Symp. Proc. 376 (1995) 499–504.
[22] P. Faucon, T. Charpentier, A. Nonat, J.C. Petit, Triple-quantum two-dimensional ^{27}Al magic angle nuclear magnetic resonance study of the aluminum incorporation in calcium silicate hydrates, J. Am. Chem. Soc. 120 (1998) 12075–12082.
[23] S. Diamond, Aspects of concrete porosity revisited, Cem. Concr. Res. 29 (1999) 1181–1188.
[24] F. Adenot, L. Auvray, J.C. Touray, Determination of the fractal dimension of CSH aggregates (hydrated calcium silicates) of different origins and compositions. Consequences for studies of cement paste durability, C. R. Acad. Sci., Ser. II 317 (1993) 185–189.
[25] A. Heinemann, H. Hermann, K. Wetzig, F. Haussler, H. Baumbach, M. Kroning, Fractal microstructures in hydrating cement paste, J. Mater. Sci. Lett. 18 (1999) 1413–1416.
[26] J.A. Janik, W. Kurdowski, R. Podsiadly, J. Samseth, Studies of fractal aspects of cement, Acta Phys. Pol., A 90 (1996) 1179–1184.
[27] H.D. Chapman, Cation-exchange capacity, in: C.A. Black (Ed.), Agronomy. Methods of Soil Analysis—Chemical and Microbiological Properties, Amer. Soc. Agron., Madison, Wisconsin, 1965, pp. 891–901.
[28] C.J. Glinka, J.G. Barker, B. Hammouda, S. Krueger, J.J. Moyer, W.J. Orts, The 30 m small-angle neutron scattering instruments at the National Institute of Standards and Technology, J. Appl. Crystallogr. 31 (1998) 430–445.
[29] A.R. Drews, J.G. Barker, C.J. Glinka, M. Agamalian, Development of a thermal-neutron double-crystal diffractometer for USANS at NIST, Physica, B 241 (1998) 189–191.
[30] NIST SANS data reduction software, 1998.
[31] NIST USANS data reduction software ver. 1, 2001.
[32] M. JCPDS, Powder Diffraction File, Alphabetical Index, Inorganic Phases, International Centre for Diffraction Data, Swarthmore, PA, 1998.
[33] D. Winslow, The fractal arrangement of hydrated cement paste, Cem. Concr. Res. 25 (1995) 147–156.

[34] S.K. Sinha, T. Freltoft, J. Kjems, Observation of power–law correlations in silica-particle aggregates by small-angle neutron scattering, in: F. Family, D.P. Landau (Eds.), Proceedings of the International Conference Kinetics of Aggregation and Gelation, Elsevier, Amsterdam, 1984, pp. 87–90.
[35] A.J. Allen, R.C. Oberthur, D. Pearson, P. Schofield, C.R. Wilding, Development of the fine porosity and gel structure of hydrating cement systems, Philos. Mag., B 56 (1987) 263–288.
[36] P.W. Schmidt, Small-angle scattering studies of disordered, porous and fractal systems, J. Appl. Crystallogr. 24 (1991) 414–435.
[37] A. Guinier, G. Fournet, Small-angle scattering of X-rays, Structure of Matter Series, Wiley, New York, 1955, p. 268.
[38] J.G. Barker, Some Effects of Multiple Scattering Encountered in SANS, 2001, unpublished.
[39] P. Debye, R. Anderson, H. Brumberger, Scattering by an inhomogeneous solid. II. The correlation function and its application, J. Appl. Phys. 28 (1957) 679–683.
[40] P. Debye, A.M. Bueche, Scattering by an inhomogeneous solid, J. Appl. Phys. 20 (1949).
[41] T.M. Sabine, W.K. Bertram, The use of multiple-scattering data to enhance small-angle neutron scattering experiments, Acta Crystallogr., A Found. Crystallogr. 55 (1999) 500–507.
[42] L.P. Aldridge, W.K. Bertram, T.M. Sabine, A. Ioffe, Microstructure of a slag-cement paste determined by small angle neutron scattering, Mater. Res. Soc. Symp. Proc. 506 (1998) 521–528.
[43] D.L. Dexter, W.W. Beeman, Multiple diffuse small angle scattering of X-rays, Phys. Rev. 76 (1949) 1782–1786.
[44] J. Schelten, W. Schmatz, Multiple-scattering treatment for small-angle scattering problems, J. Appl. Crystallogr. 13 (1980) 385–390.
[45] J.W. Phair, J.S.J. Van Deventer, Effect of silicate activator pH on the leaching and material characteristics of waste-based inorganic polymers, Miner. Eng. 14 (2001) 289–304.
[46] J.W. Phair, J.S.J. Van Deventer, J.D. Smith, Mechanism of polysialation in the incorporation of zirconia into fly ash based geopolymers, Ind. Eng. Chem. Res. 39 (2000) 2925–2934.
[47] H.F.W. Taylor, The Chemistry of Cements, Academic Press, London, 1964, p. 250.
[48] K.A. Hardman-Rhyne, N.F. Berk, Characterization of alumina powder using multiple small-angle neutron scattering. II. Experiment, J. Appl. Crystallogr. 18 (1985) 473–479.